

All electroweak four fermion processes in electron-positron collisions *

F.A. Berends[†] and R. Pittau[‡]
Instituut-Lorentz, Leiden, The Netherlands
R. Kleiss[§]
NIKHEF-H, Amsterdam, The Netherlands
May 6, 2004

Abstract

This paper studies the electroweak production of all possible four fermion states in e^+e^- collisions. Since the methods employed to evaluate the complete matrix elements and phase space are very general, all four fermion final states in which the charged particles are detected can be considered. Also all kinds of experimental cuts can be imposed. With the help of the constructed event generator a large number of illustrative results is obtained, which show the relevance of backgrounds to a number of signals. For LEP 200 the W-pair signal and its background are discussed, for higher energies also Z-pair and single W and Z signals and backgrounds are presented.

*This research has been partly supported by EU under contract number CHRX-CT-0004.

[†]email address: berends@rulgm0.LeidenUniv.nl

[‡]email address: pittau@rulgm0.LeidenUniv.nl

[§]email address: t30@nikhef.nikhef.nl

1 Introduction

In electron-positron collisions at a few hundred GeV, various gauge-boson production processes will be studied. At LEP 200, the reaction

$$e^+ e^- \rightarrow W^+ W^- \quad (1)$$

will be measured, while at somewhat higher energies also

$$e^+ e^- \rightarrow Z Z \ , \quad (2)$$

$$e^+ e^- \rightarrow W e \nu_e \ , \quad (3)$$

$$e^+ e^- \rightarrow Z e^+ e^- \ , \quad (4)$$

$$e^+ e^- \rightarrow Z \nu_e \bar{\nu}_e \ , \quad (5)$$

will come under consideration. The double-gauge boson cross sections decrease, but the single-gauge boson ones slowly increase, with increasing beam energy. Around 500 GeV, the cross sections for (1), (3) and (4) all have about the same magnitude, while those for (2) and (5) are lower by roughly an order of magnitude [1] (it should be noted that there exists a number of rarer processes in which a single vector boson is produced).

At LEP 200, the process (1) will be used for an accurate measurement of the W mass [2]. Another issue is the test of the non-Abelian couplings in reaction (1), and, at higher energies, also in the other processes. The effects of non-standard couplings between the gauge-bosons have been extensively discussed in the literature [3]. These involve terms additional to the standard non-Abelian vertices, as well as altogether new vertices, like $ZZ\gamma$, that would also affect processes independent of non-Abelian couplings such as (2) and (4).

It is clear, that for these studies accurate predictions for the cross sections (1)-(5) are needed. Therefore, the effects of radiative corrections should be known. Again, a number of such studies is available [4, 5]. For W -pair production, the radiative corrections have been studied most completely. Corrections for the total cross section range from -20 to +3 per cent when the collision energy increases from 170 to 500 GeV [4].

In addition to the radiative corrections, there is another problem. The actually measurable final states in the above reactions are not the gauge bosons themselves, but rather their decay products. Thus, all the above

reactions are just special cases of

$$e^+ e^- \rightarrow 4 \text{ fermions} . \quad (6)$$

To a specific final state, many Feynman diagrams can contribute. Some of them are related to the reactions (1)-(5); others are not. To distinguish them, they will be called *signal* and *background* diagrams, respectively. The physics issues mentioned above necessitate a good knowledge of the relative importance of signal and background diagrams. It may also happen, that different four-fermion processes lead to the same *detectable* final state as does the signal. Such a process will be called a *non-interfering* background.

The aim of this paper is to investigate, at tree level, the contribution of signal and background diagrams to the various four-fermion final states. In its full generality, this task is complicated for two reasons.

One reason is that, for a specified final state, the number of Feynman diagrams can be quite large. The matrix elements then become complicated, and we need an efficient method to compute them. In the present paper, spinorial techniques for helicity amplitudes [6]-[8] are used. Such techniques are most efficient when the fermions are massless. Since we are primarily interested in final-state configurations where charged leptons are visible at (relatively) large angles to the beams and between each other, collinear situations are absent. We therefore assume all the fermions to be massless. Note that this implies the *absence* of diagrams where a Higgs boson couples to the fermions; but, although we cannot compute Higgs signals in our approach, we can at least reliably estimate the background.

The second complication arises from the peaking structure. There are many different peaks in the multidifferential cross section, each of which finds its best description in terms of a characteristic variable. Hence, the number of characteristic variables may be much larger than the number of independent kinematical variables. We solve this problem by using a multichannel Monte Carlo method [9, 10]. The result of our work, then, is an event generator for four-fermion final states.

The Monte Carlo method allows us to evaluate four-fermion cross sections under the imposition of all kinds of cuts. In this paper, we shall do this for a number of illustrative examples, indicating the effects of the backgrounds on the measured signals. For realistic experimental situations, other effects, like

quark fragmentation and hadronization, as well as detector characteristics, must be considered. Nevertheless, the examples below already show that background diagrams can contribute 4 to 10 per cent to certain four-fermion final states.

It should be noted that the literature contains a number of papers [11]-[14] where also background effects are calculated. None of these considers all possible final states. Moreover, our emphasis on obtaining an efficient event generator allows for more experimentally precise cross section estimates than the results under necessarily simplified phase-space cuts.

The outline of the paper is as follows. Section 2 lists *all* four-fermion final states for e^+e^- collisions, together with the number of Feynman diagrams. The next section describes the matrix element computation. In section 4, the phase-space distributions are discussed, and illustrative examples of various cross sections are given in section 5. In the last section, we summarize our conclusions. In an appendix toy model cross sections are given, which serve as checks and estimates of phase space integrals.

2 Signals and Backgrounds

Since the W^\pm and Z decay into leptons and quarks, one may classify the four-fermion final states into leptonic, semileptonic and hadronic final states. The following decays for the W^+ and Z are considered:

$$W^+ \rightarrow e^+\nu_e, \mu^+\nu_\mu, \tau^+\nu_\tau, \quad (7)$$

$$W^+ \rightarrow u\bar{d}, c\bar{s}, \quad (8)$$

$$Z \rightarrow e^+e^-, \mu^+\mu^-, \tau^+\tau^-, \nu_e\bar{\nu}_e, \nu_\mu\bar{\nu}_\mu, \nu_\tau\bar{\nu}_\tau, \quad (9)$$

$$Z \rightarrow u\bar{u}, d\bar{d}, c\bar{c}, s\bar{s}, b\bar{b}. \quad (10)$$

In principle, the W knows more quark decays than (8). Those that involve a b quark are extremely rare, and can safely be neglected. The decay $u\bar{s}$ can, usually, experimentally not be distinguished from $u\bar{d}$; and the same holds for $c\bar{s}$ and $c\bar{d}$. The unitarity of the Cabibbo matrix therefore ensures that the use of only (8) will give the experimentally relevant predictions correctly.

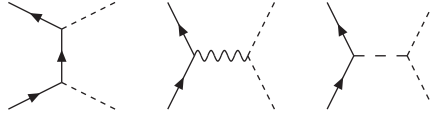


Figure 1: signal diagrams for $e^+e^- \rightarrow W^+W^-$. Here, and in the following figures, solid arrowed lines stand for fermions, dotted lines denote W 's, dashed lines Z 's, and wavy lines stand for photons.

The diagrams for the reactions (1)-(5) are given in figs.1-5. In these diagrams, the vector bosons are assumed to be stable. It is convenient to use names for certain types of diagrams, as they usually show a characteristic peaking behaviour. The first diagram of fig.1 is called a *conversion* diagram, and the other ones in fig.1 are called *annihilation* diagrams. Thus, ZZ production (fig.2) consists of conversion diagrams only, whereas Ze^+e^- has two conversion diagrams.

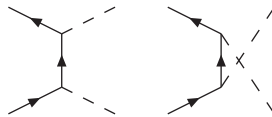


Figure 2: signal diagrams for $e^+e^- \rightarrow ZZ$.

In single W production we encounter new types of diagrams. The first and second diagram of fig.3 is called a *fusion* diagram, the next 4 ones are called *bremsstrahlung* diagrams. The latter represent bremsstrahlung of (in this case) a W from Bhabha-like scattering. Similar bremsstrahlung graphs (now with a Z radiated off) occur in single Z production, depicted in fig.4.

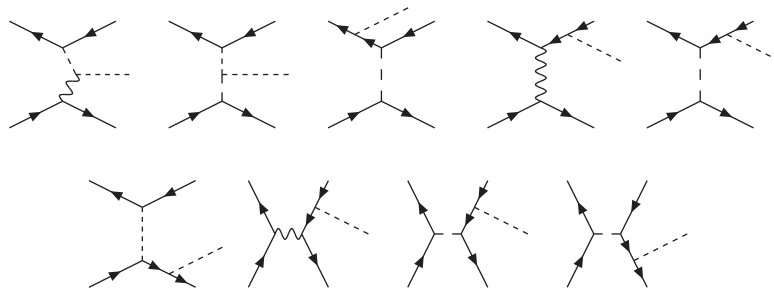


Figure 3: signal diagrams for $e^+e^- \rightarrow W^+e^-\bar{\nu}_e$

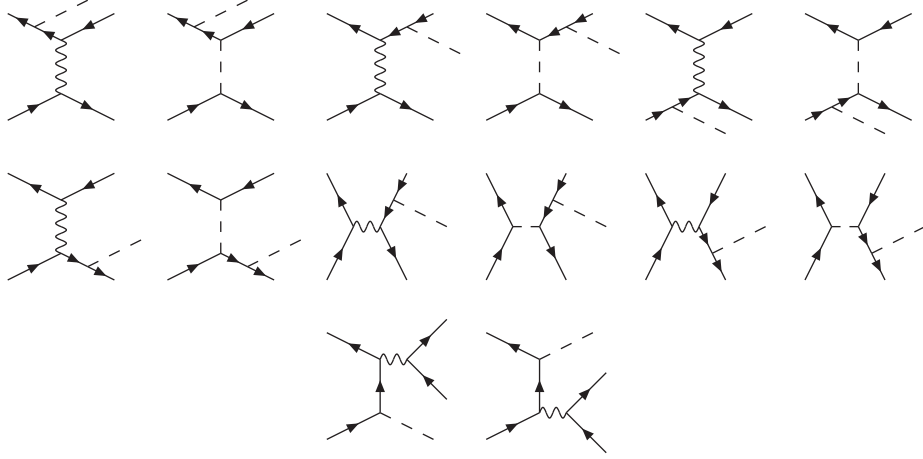


Figure 4: signal diagrams for $e^+e^- \rightarrow Ze^+e^-$

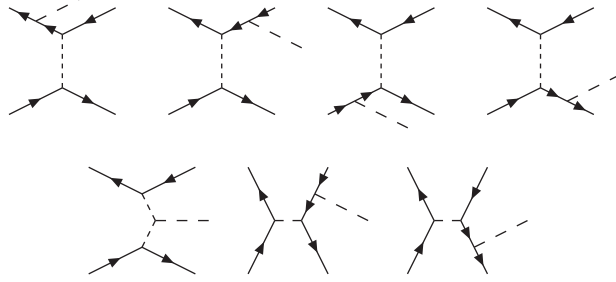


Figure 5: signal diagrams for $e^+e^- \rightarrow Z\nu_e\bar{\nu}_e$

Note that there is a number of other single W or Z production processes. They are of the form

$$e^+e^- \rightarrow \mu^- \bar{\nu}_\mu W^+ , \quad (11)$$

$$e^+e^- \rightarrow d \bar{u} W^+ , \quad (12)$$

$$e^+e^- \rightarrow \mu^+ \mu^- Z , \quad (13)$$

$$e^+e^- \rightarrow \nu_\mu \bar{\nu}_\mu Z , \quad (14)$$

$$e^+e^- \rightarrow q \bar{q} Z . \quad (15)$$

These reactions receive contributions from the annihilation graphs of figs.3-5. Reactions (13) and (15) are also possible through the conversion diagrams of fig.4.

When the bosons decay, one gets the four-fermion final states. In figs.1-5 the decay fermions are attached to the external gauge bosons. In cases with identical fermions, more diagrams can arise. For instance, when both Z 's decay into e^+e^- , fig.2 will lead to 4 diagrams. Besides the signal diagrams of figs.1-5, there are always a number of background diagrams. The largest numbers occur for $e^+e^+e^-e^-$ and $e^+e^-\nu_e\bar{\nu}_e$, the former with only neutral-current interactions. The background for $e^+e^-\nu_e\bar{\nu}_e$ contains two bremsstrahlung graphs, one fusion graph, and 9 *multiperipheral* diagrams (fig. 6).

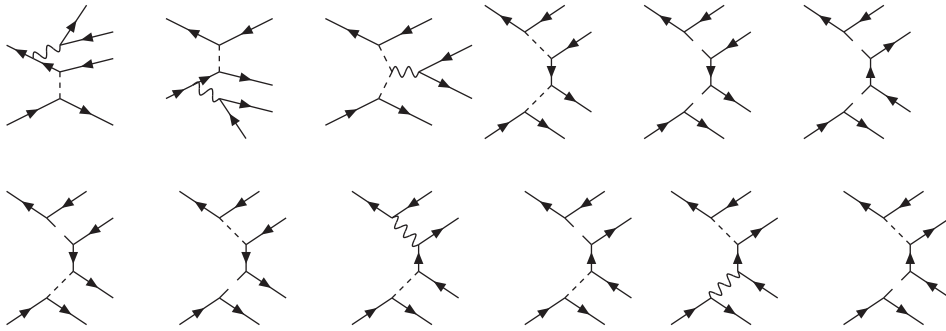


Figure 6: background diagrams for $e^+e^- \rightarrow e^+e^-\nu_e\bar{\nu}_e$

For the $e^+e^+e^-e^-$ final state, there are 32 bremsstrahlung diagrams, 4 conversion, 16 annihilation, and 32 multiperipheral ones. Of these, fig.7 depicts 21 only; the other ones are obtained by permuting the outgoing positrons or electrons.

Since different final states select different sets of diagrams, an inventory is made in tables 1-3. All final states that have the same matrix element are grouped together. Moreover, the number of Abelian diagrams (N_a) and of non-Abelian diagrams (N_n) is given. We also indicate which of the signals (1=(1),... ,5=(5)) lead to the final state, and how many of the background diagrams of figs.6 or 7 occur (N_b). It is seen, that for the leptonic processes there are 15 different matrix elements, for the semileptonic processes 10, and in the purely hadronic case 7. Since differences in the latter two cases partly arise from different quark coupling constants, the numbers of *structurally* different matrix elements in these two cases are 6 and 4, respectively.

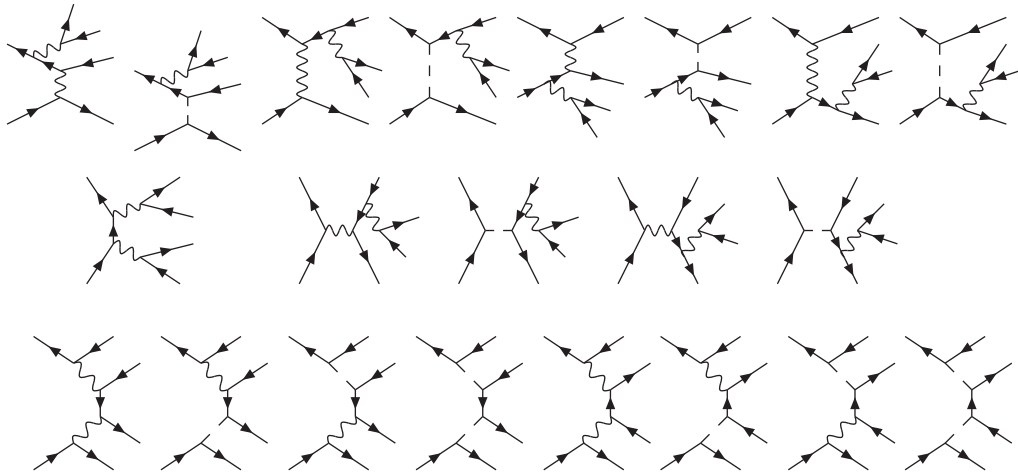


Figure 7: background diagrams for $e^+e^- \rightarrow e^+e^-e^+e^-$

3 The matrix elements

The amplitudes receive contributions from Abelian and non-Abelian graphs, with distinct topological structure. They are given in fig. 8.

In these so-called *generic* diagrams, all particles are assumed to be outgoing: assigning two fermion legs to be the initial-state fermions (by crossing), the actual Feynman diagrams are generated. In the Abelian diagrams the charges of the fermions determine the character of the two exchanged bosons, which may be W^+ , W^- , Z or γ . In the non-Abelian diagrams, two of the vector bosons are fixed to be W^+ and W^- , and the third one can be Z or γ . In this way we avoid double-counting of diagrams.

The particles and antiparticles can each be assigned in six ways to the external lines (in principle). This gives, for the Abelian graphs, a maximum of 144 different diagrams, and at most 8 for the non-Abelian diagrams.

We evaluate the matrix element at the level of helicity amplitudes. For a specific particle/antiparticle content of the final state, the contributing diagrams are enumerated by permuting the assignments of the external legs in the generic diagrams, and by relating the charges of the fermions to those of the vector bosons V_1 and V_2 .

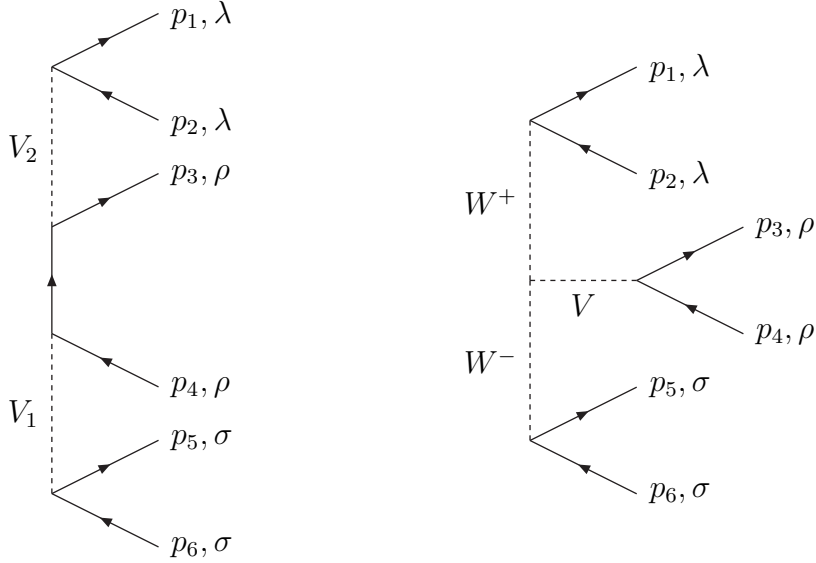


Figure 8: generic diagrams for four-fermion production. The fermion momenta and helicities, and the bosons are indicated. The bosons $V_{1,2}$ can be either Z , W^\pm , or γ ; V can be either Z or γ .

Not all of these generated diagrams will contribute to each helicity amplitude, as can be seen from the following expression for the numerator of the abelian diagram of fig.8:

$$\begin{aligned}
A(\lambda, \rho, \sigma; p_1, p_2, p_3, p_4, p_5, p_6) &= \\
&= \bar{u}_\lambda(p_1) \gamma^\mu u_\lambda(p_2) \\
&\quad \times \bar{u}_\rho(p_3) \gamma_\mu (\not{p}_1 + \not{p}_2 + \not{p}_3) \gamma_\nu u_\rho(p_4) \\
&\quad \times \bar{u}_\sigma(p_5) \gamma^\nu u_\sigma(p_6) .
\end{aligned} \tag{16}$$

Here we have disregarded the particle/antiparticle distinction since it is already implied by the assignment of the external momenta. The helicity labels $\lambda, \rho, \sigma = \pm$ determine the helicity of both external legs on a given fermion line. Using the Weyl-van der Waerden formalism for helicity amplitudes [8] (or, equivalently, the Dirac formalism of [7]), the expression A can easily be calculated. For instance, for $\lambda = \rho = \sigma = 1$ one finds

$$A(+, +, +; 1, 2, 3, 4, 5, 6) = -4\langle 31 \rangle^* \langle 46 \rangle [\langle 51 \rangle^* \langle 21 \rangle + \langle 53 \rangle^* \langle 23 \rangle] , \tag{17}$$

where the spinorial product is given, in terms of the momenta components, by

$$\langle kj \rangle \equiv (p_j^1 + ip_j^2) \left[\frac{p_k^0 - p_k^3}{p_j^0 - p_j^3} \right]^{1/2} - (k \leftrightarrow j) . \quad (18)$$

we denote the expression of Eq.(17) by $A_0(1, 2, 3, 4, 5, 6)$. All helicity combinations can be expressed in terms of A_0 , as follows:

$$\begin{aligned} A(+++) &= A_0(1, 2, 3, 4, 5, 6) & A(- - -) &= A_0(1, 2, 3, 4, 5, 6)^* , \\ A(-++) &= A_0(2, 1, 3, 4, 5, 6) & A(+ - -) &= A_0(2, 1, 3, 4, 5, 6)^* , \\ A(++-) &= A_0(1, 2, 3, 4, 6, 5) & A(- - +) &= A_0(1, 2, 3, 4, 6, 5)^* , \\ A(-+-) &= A_0(2, 1, 3, 4, 6, 5) & A(+ - +) &= A_0(2, 1, 3, 4, 6, 5)^* . \end{aligned} \quad (19)$$

The numerator in the non-Abelian diagrams can also be written in terms of the function A :

$$\begin{aligned} & \bar{u}_\lambda(p_1)\gamma_\alpha u_\lambda(p_2) \bar{u}_\rho(p_3)\gamma_\mu u_\rho(p_4) \bar{u}_\sigma(p_5)\gamma_\nu u_\sigma(p_6) \\ & \times \{g^{\mu\alpha}(p_1 + p_2)^\nu + g^{\alpha\nu}(p_5 + p_6)^\mu + g^{\nu\mu}(p_3 + p_4)^\alpha\} \\ & = A(\lambda, \rho, \sigma; 1, 2, 3, 4, 5, 6) - A(\sigma, \rho, \lambda; 5, 6, 3, 4, 1, 2) . \end{aligned} \quad (20)$$

Thus, for massless fermions, every helicity amplitude consists of a sum of very systematic, and relatively compact, expressions. When the fermions acquire a non-zero mass, the spin states of the external legs are not related so simply anymore. Additional helicity amplitudes therefore occur, as well as extra terms in the ones above, that are suppressed by one and two powers of the ratio fermion mass/energy, respectively. Also, new diagrams crop up, where massive fermions are coupled to a Higgs boson. In these diagrams, the unsuppressed helicity amplitudes (that nonetheless contain the fermion mass in the coupling constant to the Higgs) are precisely the ones that are suppressed in the vector boson diagrams, and vice versa. We may therefore conclude that the interference of the Higgs diagrams with the vector boson diagrams will always be suppressed by a factor proportional to the fermion mass squared.

Finally it should be noted that the vector boson propagators are implemented in the form $q^2 - M_V^2 + iM_V\Gamma_V$, irrespective whether q is timelike or not. This only introduces a negligible error. A more refined procedure with a q^2 dependent width is of course possible.

4 The Monte Carlo

In this section we describe the structure of EXALIBUR, a Monte Carlo simulation program for the four-fermion production processes discussed above. First, we shall review the basic ideas, and then show their implementation in the actual simulation.

For the sake of simplicity let us concentrate on the total cross section σ for some process

$$e^+(p_1) e^-(p_2) \rightarrow f_1(p_3) \bar{f}_2(p_4) f_3(p_5) \bar{f}_4(p_6) . \quad (21)$$

The main formula is

$$\sigma = \int f(\vec{\Phi}) d\vec{\Phi} , \quad (22)$$

where $f(\vec{\Phi})$ denotes the matrix element squared (any cut can be easily implemented by putting $f(\vec{\Phi}) = 0$ in the unwanted region of the phase space) and

$$d\vec{\Phi} = \prod_{i=3}^6 d^4 p_i \delta(p_i^2) \delta^4(p_1 + p_2 - p_3 - p_4 - p_5 - p_6) \quad (23)$$

is the 8-dimensional massless phase space integration element.

In order to reduce the variance of the integrand, and therefore the Monte Carlo error, it is convenient to introduce an analytically integrable function $g(\vec{\Phi})$, called the *local density*, that exhibits approximately the same peaking behaviour of $f(\vec{\Phi})$ and is *unitary*, that is, a normalized probability density:

$$\int g(\vec{\Phi}) d\vec{\Phi} = 1 . \quad (24)$$

By multiplying and dividing the integrand by $g(\vec{\Phi})$, the cross section can be rewritten as follows

$$\sigma = \int w(\vec{\Phi}(\vec{\rho})) d\vec{\rho} \quad (25)$$

where the new integrand

$$w(\vec{\Phi}(\vec{\rho})) = \frac{f(\vec{\Phi})}{g(\vec{\Phi})} \quad (26)$$

is a smoother function of the new set of variables $\{\rho_i\}$ defined by

$$\begin{aligned} d\vec{\rho} &= g(\vec{\Phi})d\vec{\Phi} \\ 0 &< \rho_i < 1 \end{aligned} \tag{27}$$

so that the variance of $w(\vec{\rho})$ is smaller than the variance of $f(\vec{\Phi})$.

When the peaking structure of the matrix element squared is very rich (the worst case being $e^+e^- \rightarrow e^+e^-e^+e^-$ with 144 different Feynman diagrams) one set of new integration variables $\{\rho_i\}$ can only describe well a limited number of peaks. Therefore a multichannel approach is required in which

$$g(\vec{\Phi}) = \sum_{i=1}^N \alpha_i g_i(\vec{\Phi}) \ , \quad \sum_{i=1}^N \alpha_i = 1 \ , \quad \int g_i(\vec{\Phi})d\vec{\Phi} = 1 \ , \tag{28}$$

and where every $g_i(\vec{\Phi})$ describes a particular peaking structure of $f(\vec{\Phi})$. Note that the conditions on the α_i and $g_i(\vec{\Phi})$ ensure unitarity of the algorithm, *i.e.* probability is explicitly conserved at each step of the algorithm, without additional normalization factors at any stage.

The numbers α_i are called *a-priori weights* and, although their numerical values are in principle unimportant, they can be used, in practice, to reduce the Monte Carlo error [10].

In EXCALIBUR we have dealt with the problem of the construction of the $g_i(\vec{\Phi})$ in a very modular and systematic way. Firstly we have singled out all possible kinematical diagrams¹ for every four-fermion final state. Secondly we have constructed all building blocks (that is subroutines) necessary for the calculation. Finally we have put them together to form the $g_i(\vec{\Phi})$.

To illustrate the outlined procedure we shall treat in detail one particular channel, that is the conversion channel with one massless and one massive particle emitted.

Referring to the kinematical diagram in figure 9, a suitable choice for the 8 integration variables is

- the angle θ between p_1 and $p_3 + p_4$ in the lab frame;

¹Here and in the following kinematical diagrams are defined to be pictures that represent the various peaking structures. Although they are inspired by the Feynman diagrams, they should not be interpreted further than that they indicate which variables are most appropriate to a given $g_i(\vec{\Phi})$ [10].

- the azimuthal angle ϕ adjoint to θ ;
- the decay angle θ_1 of the particles 3 and 4 in the rest frame of $(p_3 + p_4)$, and its adjoint ϕ_1 ;
- the decay angle θ_2 of the particles 5 and 6 in the rest frame of $(p_5 + p_6)$, and its adjoint ϕ_2 ;
- the squared invariant masses $s_{34} = (p_3 + p_4)^2$ and $s_{56} = (p_5 + p_6)^2$.

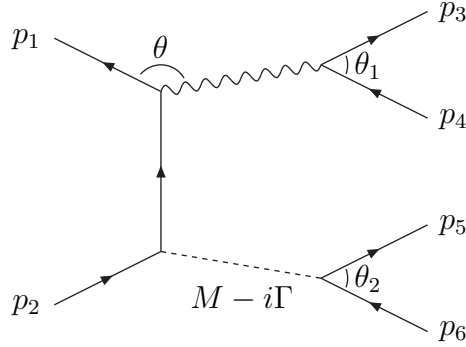


Figure 9: kinematical diagram representing a conversion with emission of one massless and one massive particle.

Furthermore we expect in the cross section $\cos \theta$ distributed like

$$\frac{1}{(a - \cos \theta)^\nu} \quad , \quad \nu \sim 1 \quad , \quad a = \frac{\sqrt{s}(E_3 + E_4) - s_{34}}{\sqrt{s}|\vec{p}_3 + \vec{p}_4|} \quad , \quad (29)$$

s_{34} like

$$\frac{1}{s_{34}^{\nu_1}} \quad , \quad \nu_1 \sim 1 \quad , \quad (30)$$

and s_{56} like

$$\frac{1}{(s_{56} - M^2)^2 + M^2\Gamma^2} \quad , \quad (31)$$

while all other distributions are expected to be more or less flat. Therefore the phase space integration can be split into five parts. Using

$$\begin{aligned} 1 &= \int ds_{34} d^4 P_{34} \delta^4(P_{34} - p_3 - p_4) \delta((p_3 + p_4)^2 - s_{34}) \quad , \\ 1 &= \int ds_{56} d^4 P_{56} \delta^4(P_{56} - p_5 - p_6) \delta((p_5 + p_6)^2 - s_{56}) \quad (32) \end{aligned}$$

it follows

$$\begin{aligned}
\int d\vec{\Phi} &= \underbrace{\int_{s_{min}}^s \frac{ds_{34}}{s_{34}^{\nu_1}} \cdot s_{34}^{\nu_1}}_i \\
&\quad \underbrace{\int_0^{(\sqrt{s}-\sqrt{s_{34}})^2} \frac{ds_{56}}{[(s_{56}-M^2)^2+M^2\Gamma^2]} \cdot [(s_{56}-M^2)^2+M^2\Gamma^2]}_{ii} \\
&\quad \times \underbrace{\frac{1}{8}\lambda^{\frac{1}{2}}\left(\frac{s_{34}}{s}, \frac{s_{56}}{s}\right) \int_0^{2\pi} d\phi \int_{-1}^1 \frac{d\cos\theta}{(a-\cos\theta)^\nu} \cdot (a-\cos\theta)^\nu}_{iii} \\
&\quad \times \underbrace{\frac{1}{8} \int_0^{2\pi} d\phi_1 \int_{-1}^1 d\cos\theta_1}_{iv} \quad \underbrace{\frac{1}{8} \int_0^{2\pi} d\phi_2 \int_{-1}^1 d\cos\theta_2}_v
\end{aligned} \tag{33}$$

where s_{min} is a minimum value for s_{34} and

$$\lambda(x, y) = 1 + x^2 + y^2 - 2x - 2y - 2xy . \tag{34}$$

The first and the second contributions take care of the photon and the massive boson propagators, the third one describes the t -channel distribution of $\cos\theta$ while the last two integrals represent the two body decays of the massless and massive boson respectively. The new set of integration variables $\{\rho_i\}$ is

$$\begin{aligned}
s_{34} &= [\rho_1 s^{(1-\nu_1)} + (1-\rho_1) s_{min}^{(1-\nu_1)}]^{\frac{1}{1-\nu_1}} , \\
s_{56} &= M^2 + M\Gamma \tan[\rho_2(y^+ - y^-) + y^-] , \\
y^+ &= \tan^{-1} \left[\frac{(\sqrt{s} - \sqrt{s_{34}})^2 - M^2}{M\Gamma} \right] , \\
y^- &= \tan^{-1}(-M/\Gamma) , \\
\phi &= 2\pi\rho_3 , \\
\cos\theta &= a - [\rho_4(a-1)^{(1-\nu_1)} + (1-\rho_4)(a+1)^{(1-\nu_1)}]^{\frac{1}{1-\nu_1}} , \\
\phi_1 &= 2\pi\rho_5 , \\
\cos\theta_1 &= 2\rho_6 - 1 , \\
\phi_2 &= 2\pi\rho_7 , \\
\cos\theta_2 &= 2\rho_8 - 1 ,
\end{aligned} \tag{35}$$

so that it is possible to rewrite

$$\begin{aligned}
\int d\vec{\Phi} &= \int_0^1 \prod_{i=1}^8 d\rho_i \underbrace{s_{34}^{\nu_1}}_{g_i^{-1}} \underbrace{[(s_{56} - M^2)^2 + M^2\Gamma^2]}_{g_{ii}^{-1}} \\
&\times \underbrace{\frac{\pi}{4} \lambda^{\frac{1}{2}} \left(\frac{s_{34}}{s}, \frac{s_{56}}{s} \right)}_{g_{iii}^{-1}} \underbrace{(a - \cos \theta)^\nu}_{g_{iv}^{-1}} \underbrace{\frac{\pi}{2}}_{g_v^{-1}} \underbrace{\frac{\pi}{2}}_{g_v^{-1}} , \quad (36)
\end{aligned}$$

Therefore the total local density can be written as a product of five contributions

$$g(\vec{\Phi}) = g_i \cdot g_{ii} \cdot g_{iii} \cdot g_{iv} \cdot g_v . \quad (37)$$

The advantage of this splitting is that every part of the algorithm can be used again for other channels, both to generate distributions through eqs.(35) and to compute local densities. For example, using the same ingredients, the channel in figure 10 can be easily built as follows

$$\begin{aligned}
\int d\vec{\Phi} &= \underbrace{\int_0^s \frac{ds_{56}}{[(s_{56} - M^2)^2 + M^2\Gamma^2]} \cdot [(s_{56} - M^2)^2 + M^2\Gamma^2]}_{ii} \\
&\times \underbrace{\int_{s_{56}}^s \frac{ds_{456}}{s_{456}^{\nu_1}} \cdot s_{456}^{\nu_1}}_i \\
&\times \underbrace{\frac{1}{8} \lambda^{\frac{1}{2}} \left(\frac{s_3}{s}, \frac{s_{456}}{s} \right) \int_0^{2\pi} d\phi \int_{-1}^1 \frac{d \cos \theta}{(1 - \cos \theta)^\nu} \cdot (1 - \cos \theta)^\nu}_{iii} \\
&\times \underbrace{\frac{1}{8} \int_0^{2\pi} d\phi_1 \int_{-1}^1 d \cos \theta_1}_{iv} \underbrace{\frac{1}{8} \int_0^{2\pi} d\phi_2 \int_{-1}^1 d \cos \theta_2}_v \quad (38)
\end{aligned}$$

where $s_3 = p_3^2$, $s_{456} = (p_4 + p_5 + p_6)^2$ and (θ_1, ϕ_1) , (θ_2, ϕ_2) are the decay angles of s_{456} and s_{56} .

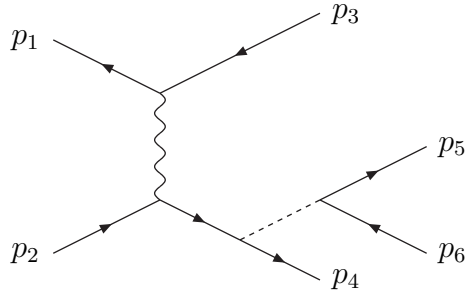


Figure 10: kinematical diagram representing a decaying massive boson radiated off a final leg.

This finishes our description of the event generation procedure. More details can be found elsewhere [16]. Finally, a brief remark is in order on the collinear singularity in the multiperipheral and bremsstrahlung diagrams. Consider an incoming electron with momentum p^μ , which scatters over a small angle into an outgoing momentum q^μ , by emitting a photon with virtuality t . We then have

$$t = (p - q)^2 = 2m_e^2 - 2p^0 q^0 + 2|\vec{p}||\vec{q}| \cos \theta \quad (39)$$

where θ is the scattering angle. For very small scattering angles, the cross section will indeed be dominated by the Feynmann diagrams with this multiperipheral structure. If the electron is massive, there is no singularity, in the sense that

$$t < t_0 \quad (40)$$

$$t_0 = 2(m_e^2 - p^0 q^0 + |\vec{p}||\vec{q}|) \sim -\frac{m_e^2(p_0 - q_0)^2}{p_0 q_0} \quad (41)$$

where we have assumed $m_e \ll q_0, p_0$. The total cross section is therefore finite. For massless electrons this is not the case because the collinear singularity can be reached. We may, however, mimic the dominant effects of a nonzero mass by imposing, on the generated event, a cut

$$\theta > \theta_0(p_0, q_0) \quad (42)$$

$$\theta_0(p_0, q_0) = \frac{m_e(p_0 - q_0)}{p^0 q^0} . \quad (43)$$

This cut leads, for massless electrons, to the same limit, t_0 , on t that would arise in the massive case. In our Monte Carlo approach, such a cut can be easily applied to one or to both multiperipheral legs. In fact, in the t-channel generation of θ , the value of the exponent ν in eq. 29 is arbitrary. Therefore, using $\nu < 1$, $\cos\theta$ can be generated in its full range $[-1,1]$ even in the case of massless particles and any final state dependent cut implemented in an event by event basis. Note, however, that this procedure only reproduces the leading log result of the full, massive, cross section. For instance, subleading terms due to spin-flip amplitudes are necessarily absent. On the other hand, the angle θ_0 is typically much smaller than any detector is likely to cover, so the kinematics of the final state are, for all practical purposes, those of the massless electron cross section.

5 Results

In this section we present some illustrative examples of the physics results one can obtain with the event generator. The input parameters used are the masses and widths of the gauge bosons and the electroweak couplings parametrized by α and $\sin^2\theta_W$. The masses and the widths are taken to be independent parameters. The actual values in the program are $\alpha = 1/129$, $\sin^2\theta_W = 0.23$, $M_W = 80.5$, $\Gamma_W = 2.3$, $M_Z = 91.19$ and $\Gamma_Z = 2.5$ (all GeV). Note that, for simplicity, we have obtained results for fixed, energy-independent widths. The change to s-dependent widths is trivial by a simple modification of the boson propagators computed for each Monte Carlo event. There are three types of results. The first type consists of checks against other calculations. The second type is concerned with W-pair production at LEP 200 and somewhat higher energies. The third type is related to high energy results for a future linear e^+e^- collider and illustrates signal/background issues for all five signals.

As to the checks of the program, we first have verified that all toy model matrix elements described in the appendix are, in fact, correctly computed by the program. This serves to establish the consistency and reliability of our approach. As to more physically meaningful comparisons, results of the generator for the W-pair signal have been obtained for a number of decreasing widths. The extrapolated values compare well with the zero width analytic result (table 4). In order to compare with a more complicated set of

diagrams the semileptonic channel $\mu^-\bar{\nu}_\mu u\bar{d}$ was chosen for which an analytic calculation exists [15]. Both the full calculation with all diagrams and the signal calculation agree within the errors of the Monte Carlo calculation.

The LEP 200 results are divided up into leptonic, semileptonic and hadronic final states.

As for the leptonic final states, results for two charged leptons and two neutrinos are collected in table 5. The first entry is the W-pair signal, then the final states 1,6,16,20,18,2 and 8 of table 1 follow. They are calculated for all diagrams. Reactions 16,18 and 20 are the non-interfering backgrounds.

Focussing on the results for a c.m.s. energy of 200 GeV, we see that taking into account all diagrams for the final states $e^+e^-\nu_e\bar{\nu}_e$, $e^-\bar{\nu}_e\nu_\mu\mu^+$, $\mu^+\mu^-\nu_\mu\bar{\nu}_\mu$, $\mu^-\bar{\nu}_\mu\nu_\tau\tau^+$ gives generally speaking a larger cross section than the W-pair diagrams alone. One finds increases of 12, 3, 5, 0 % respectively. The non-interfering backgrounds to the e^+e^- final state add up to 9.5 % of the WW signal and for the $\mu^+\mu^-$ or $\tau^+\tau^-$ final state to 9%.

For completeness we note that there is also an invisible 4 neutrino cross section. Without any cuts it has at 200 GeV the value $.8035 \cdot 10^{-1}$ pb, to be compared with the total 2 neutrino cross section of 41.82 pb.

The semileptonic states related to the W-pair signal are final states 1 and 5 of table 2. The results involving only the signal diagrams and those containing all diagrams are listed in table 6. Inclusions of all diagrams for the $e^-\bar{\nu}_e u\bar{d}$ final state gives an increase of 4 % above the WW signal at 200 GeV. When an invariant mass cut is imposed on the quark pair, the effect does not change, while a double invariant mass cut (provided the lepton-neutrino invariant mass can be experimentally reconstructed) washes out any difference, as shown in table 7. For the $\mu^-\nu_\mu u\bar{d}$ final state there is little difference between the signal and the full calculation at LEP 200 energies.

The results for the 4 quark final states are given in table 8. The full calculation for the $u\bar{u}d\bar{d}$ final state gives an answer 3% above the signal value, again at 200 GeV. For the $u\bar{d}s\bar{c}$ there is no difference between the signal and the full calculation. When one adds all 4 jet events coming from the signal and does the same for all non-interfering backgrounds, then the latter are 8% of the real signal. Note that those are non-interfering electroweak backgrounds and not QCD backgrounds. These should be added as well, but this is beyond the scope of the present paper.

The third type of results is for energies of 500, 1000 and 2000 GeV. It should illustrate the possibilities of extracting the signal from a specific

final state, where the final state is produced by all diagrams. We take the idealized case where one could measure any invariant mass combination of the four fermions in the final state. When a charged or neutral fermion pair has an invariant mass $m_{(ij)}$ in the interval $[M_V - 2\Gamma, M_V + 2\Gamma]$ for $V = W$ or Z we identify the fermion pair as originating from the vector boson V . In table 9 the $e^- \bar{\nu}_e \nu_e e^+$ final state produced at 500 GeV is analyzed with respect to its vector boson content. There are events which do not contain any mass combination giving rise to a vector boson, but there are also some events containing apparently three vector bosons. It is now interesting to compare this analysis carried out on σ_{tot} containing all diagrams with a similar analysis on $\sigma_{(i)}$, the cross section originating from the signal diagrams for process (i). Tables 10 - 13 do this for 4 different final states. In table 10 the $e^- \bar{\nu}_e \nu_e e^+$ final state is analyzed. The cross section σ_{tot} always is greater than the sum of all signals. This demonstrates the relevance of the diagrams of fig. 6. Tables 11 - 13 consider $e^- \nu_e u \bar{d}$, $e^+ e^- u \bar{u}$ and $\nu_e \bar{\nu}_e u \bar{u}$ final states. Usually σ_{tot} is greater than $\sum_i \sigma_{(i)}$, but not always. When one applies the idealized search algorithm to σ_{tot} and to every $\sigma_{(i)}$ both σ_{tot} and $\sigma_{(i)}$ are reduced, the former of course much more drastically. The vector boson cross sections extracted from σ_{tot} tend to be greater than those originating from the signal cross section with a possible exception at 2000 GeV. The extracted WW cross sections are within the errors equal, for $Z e^+ e^-$ and $Z \nu \nu$ this is also more or less the case at 1000 and 2000 GeV.

From these idealized examples it seems that search algorithms are possible which extract the specific vector boson signal cross section. This causes a significant loss in statistics. Since most of the theoretical anomalous vector boson coupling studies have been performed for non decaying vector boson final states, one has to take into account this reduction of statistics. When one prefers to keep the higher statistics, then it seems recommendable to study the effect of non-abelian couplings directly on the four-fermion final states.

It should be noted that the energy dependences of the signals in tables 10 - 13 can differ from those in ref. [1]. The reason is that in the tables the cross sections always have some cuts on the scattering angle, whereas in [1] the full phase space has been taken into account.

6 Conclusions

In this paper one strategy is chosen for the computation of all possible four fermion final states. Whatever process is chosen the calculation proceeds through the same series of steps. On one hand, this concerns the matrix element which in principle contains all diagrams obtained by permutation from two basic diagrams. On the other hand, it means that, for a specified final state, the possible peaking structures are found and the phase space is generated accordingly. The algorithms for the generation of phase space are always made up of a particular combination of elementary building blocks. The use of one procedure for the matrix element and of a set of well tested (through model matrix elements) algorithms for distributions of certain kinematical variables makes the calculation transparent and less error prone. The neglect of fermion masses renders the computation fast when one considers the often large number of Feynman diagrams.

The four fermion final states offer a rich phenomenology: quite different pure leptonic, semi leptonic and quark final states can be studied. Moreover, the number of contributing diagrams to a specific process varies a lot. In terms of produced vector bosons, which subsequently decay, there are five signals which have been treated frequently in the literature. For these the questions of signal and background are discussed in this paper for a set of four fermion final states. It is shown that sometimes the backgrounds are of the same order of magnitude as radiative corrections and that certain experimental cuts can reduce the backgrounds. Often both signal and background are then reduced, which causes a loss in statistics. Finally, some possible future extensions of our calculation or their applications are listed

- 1) certain studies, like effects of anomalous couplings have actually been performed for vector boson final states. In view of the above losses in statistics one may consider to build in directly anomalous couplings into the matrix element of section 3;
- 2) another possibility is to use the event generator for simulating non-interfering background events for Higgs searches;
- 3) when the QCD matrix elements are also taken into account, a full analysis of four jet events in the region of vector boson production can be performed;

- 4) radiative corrections to signals and backgrounds have not been considered here. Some effects could be included in a further development of the event generator. The most important one is the initial state radiation, either in one loop or in a leading logarithmic approximation.

A last remark is in order. When one would like to study the precise effects of untagged electrons or positrons one clearly needs massive fermions in the matrix element and also an efficient algorithm for generating two photon multiperipheral diagrams in the full phase space. This problem has been dealt with in the literature in the past. It seems that one is unavoidably led to time consuming event generators. Therefore an extension of the present event generator to the exact massive fermion calculation is bound to be quite involved and conducive to an appreciable loss in program speed.

Acknowledgments

Discussions with Dr. W. Beenakker are gratefully acknowledged. We like to thank Dr. Bardin for providing us with numbers from his analytical calculations. We also thank the University of Wisconsin, in particular M. Livny et al. from the Computer Science Department, for making available computing resources at the Madison site through the Condor distributed batch system, and Dr. R. van Dantzig for his help in using the Condor facilities.

Appendix A: Model matrix elements and cross sections

It is obvious that a Monte Carlo program such as EXCALIBUR has to be tested extensively before it can be considered reliable. One of the most important kinds of tests is the Monte Carlo integration of a matrix element that, at the one hand, displays some of the salient features of the cross section, and, on the other hand, has an analytically known cross section. Note that this integral can be computed for any allowed set of a-priori weights α_i , that is, either with the Monte Carlo channel $g_i(\vec{\Phi})$ that gives the same peaking structure, or with another channel, or with any combination of channels, and in each case the correct cross section should be reproduced (with of course

a larger error if the appropriate channel is not included). Therefore, we give in this appendix a list of such model matrix elements. These can be used either for a user test of the Monte Carlo, and also (when the relevant coupling constants are added) to get a rough idea of the order of magnitude of the contribution of the various kinematical regions to the total cross section. In all cases, $p_{1,2}$ denote the incoming momenta, and $p_{3,4,5,6}$ the produced fermion momenta. Each model matrix element (squared and spin summed/averaged) is denoted by T_i , and the corresponding total cross section is

$$\tilde{\sigma}_i = \frac{1}{(2s)(2\pi)^8} \int T_i d\vec{\Phi} . \quad (44)$$

A.1 Conversion channels

We distinguish the three cases of conversion of two photons, one photon and one resonance and two resonances, respectively.

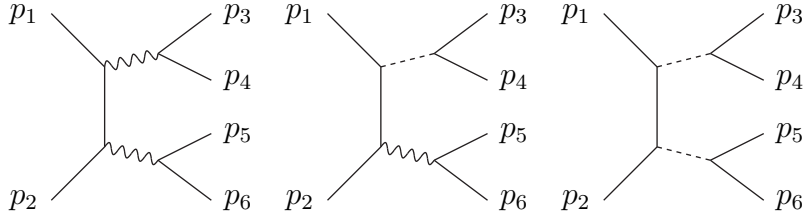


Figure 11:
two-photon
conversion

Figure 12:
photon-resonance
conversion

Figure 13:
two-resonance
conversion

For these channels we define the function

$$\begin{aligned} \tau(s_1, s_2) &= s \left[\log \left(\frac{s - s_1 - s_2 + \lambda(s, s_1, s_2)}{s - s_1 - s_2 - \lambda(s, s_1, s_2)} \right) \right]^{-1} , \\ \lambda(s, s_1, s_2) &= \left((s - s_1 - s_2)^2 - 4s_1s_2 \right)^{1/2} . \end{aligned} \quad (45)$$

This function helps us to obtain analytical closed forms for the various cross sections. Owing to the logarithm, it depends not too strongly on s_1 and s_2 .

A.1.1 Two photons

The kinematical situation is depicted in fig. 11. We have $s_1 = q_1^2 = (p_3 + p_4)^2$, $s_2 = q_2^2 = (p_5 + p_6)^2$ and $Q^\mu = p_1^\mu - q_1^\mu$. In order to avoid singularities we impose a lower bound on s_1 and s_2 , and our model for T_1 becomes

$$T_1 = \frac{\tau(s_1, s_2)}{|Q^2|} \frac{\theta(s_{1,2} > s_0)}{s_1 s_2} \quad (46)$$

and the cross section

$$\tilde{\sigma}_1 = F \left(\frac{\pi}{2} \right)^3 \left[8 \operatorname{Li}_2 \left(\frac{w_0}{w} \right) - 2 \frac{\pi^2}{3} + 4 \log^2 \left(\frac{w_0}{w} \right) \right] . \quad (47)$$

Here and in the following, the step-function θ of an inequality is 1 if the inequality holds, and 0 otherwise. Furthermore, $w = \sqrt{s}$, $w_i = \sqrt{s_i}$ ($i=0,1,2$) and $F = \frac{1}{(2s)(2\pi)^8}$.

A.1.2 One photon and one resonance

One of the photons now becomes a Breit-Wigner resonance with mass m and width Γ (see fig. 12). We may now drop the lower limit on s_1 :

$$T_2 = \frac{s \tau(s_1, s_2)}{|Q^2|} \frac{\theta(s_2 > s_0)}{R(s_1) s_2} , \quad R(s_1) = |s_1 - m^2 + im\Gamma|^2 . \quad (48)$$

The total cross section is given by

$$\begin{aligned} \tilde{\sigma}_2 &= F \left(\frac{\pi}{2} \right)^3 \frac{s}{2im\Gamma} [A_2(z) - A_2(z^*)] , \quad z = m^2 + im\Gamma \\ A_2(z) &= 2 [B_2(y) + B_2(-y)] , \quad y = \sqrt{z} \\ B_2(y) &= \log \left(\frac{w-y}{w_0} \right) \log \left(\frac{w-w_0-y}{-y} \right) \\ &\quad - \operatorname{Li}_2 \left(\frac{w-w_0-y}{w-y} \right) + \operatorname{Li}_2 \left(\frac{-y}{w-y} \right) . \end{aligned} \quad (49)$$

Evaluation of this cross section relies on the evaluation of logarithms and dilogarithms of complex arguments. Since their imaginary parts are not infinitesimal, this poses no principal difficulty.

A.1.3 Two resonances

We use, for generality, two different masses $m_{1,2}$ and widths $\Gamma_{1,2}$. Our model matrix element squared is now

$$T_3(s_1, s_2) = \frac{s^2 \tau(s_1, s_2)}{R_1(s_1)R_2(s_2)} \quad , \quad R_k(s_k) = |s_k - m_k^2 + i m_k \Gamma_k|^2 \quad (50)$$

and the total cross section $\tilde{\sigma}_3$ is quite analogous to $\tilde{\sigma}_2$;

$$\begin{aligned} \tilde{\sigma}_3 &= F \left(\frac{\pi}{2} \right)^3 \frac{-s^2}{4m_1 m_2 \Gamma_1 \Gamma_2} \\ &\quad \times [A_3(z_1, z_2) - A_3(z_1, z_2^*) - A_3(z_1^*, z_2) + A_3(z_1^*, z_2^*)] \quad , \\ z_k &= m_k^2 + i m_k \Gamma_k \quad , \\ A_3(z_1, z_2) &= B_3(y_1, y_2) + B_3(y_1, -y_2) + B_3(-y_1, y_2) + B_3(-y_1, -y_2) \quad , \\ y_k &= \sqrt{z_k} \quad , \\ B_3(y_1, y_2) &= \text{Li}_2 \left(\frac{y_2}{y_1 + y_2 - w} \right) - \text{Li}_2 \left(\frac{y_2 - w}{y_1 + y_2 - w} \right) + \log \left(1 - \frac{y_1 + y_2}{w} \right) \\ &\quad \times \left[\log \left(1 - \frac{w}{y_1} \right) + \log \left(\frac{y_1}{y_1 + y_2 - w} \right) - \log \left(\frac{y_1 - w}{y_1 + y_2 - w} \right) \right] \\ &\quad - \log \left(1 - \frac{w}{y_1} \right) \log \left(\frac{y_2}{w} \right) - \log \left(1 - \frac{y_2}{w} \right) \log \left(\frac{y_1}{y_1 + y_2 - w} \right) \\ &\quad + \log \left(-\frac{y_2}{w} \right) \log \left(\frac{y_1 - w}{y_1 + y_2 - w} \right) \quad . \end{aligned} \quad (51)$$

A.2 Non-Abelian boson fusion channels

Since the fusing bosons are in the t-channel, we neglect their Q^2 dependence if they are W or Z. This approximation is not so good if $s \gg m_{Z,W}^2$, but at LEP 200 energies it is quite accurate and, in any case, we are allowed to propose any form for T , provided it can be checked with our Monte Carlo.

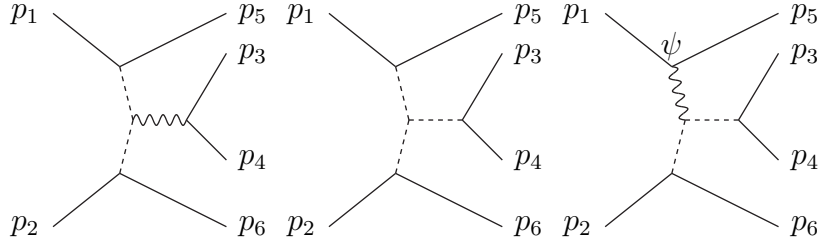


Figure 14: two heavy bosons fusing into a photon Figure 15: two heavy bosons fusing into a resonance Figure 16: boson and photon fusing into a resonance

A.2.1 Fusion of two heavy bosons into a photon

The kinematics is given in fig. 14 and we write $s_1 = (p_3 + p_4)^2$. Our model for this channel is

$$T_4 = \frac{\theta(s_1 > s_0)}{ss_1} \quad (52)$$

and the cross section evaluates to

$$\tilde{\sigma}_4 = F \left(\frac{\pi}{2} \right)^3 \frac{1}{2} \left[\left(1 + \frac{2s_0}{s} \right) \log \frac{s}{s_0} - \frac{5}{2} + \frac{2s_0}{s} + \frac{s_0^2}{2s^2} \right] . \quad (53)$$

A.2.2 Two heavy bosons fusing into a resonance

Replacing the photon of fig. 14 by a resonance, we get fig. 15 and we have

$$T_5 = \frac{1}{R(s_1)} , \quad R(s_1) = |s_1 - m^2 + im\Gamma|^2 \quad (54)$$

and

$$\begin{aligned} \tilde{\sigma}_5 &= F \left(\frac{\pi}{2} \right)^3 \frac{s}{4im\Gamma} [A_5(z) - A_5(z^*)] , \quad z = m^2 + im\Gamma \\ A_5(z) &= \left(1 - \frac{z^2}{s^2} \right) \log \left(1 - \frac{s}{z} \right) - \frac{5}{2} - \frac{z}{s} + \frac{2z}{s} \text{Li}_2 \left(\frac{s}{z} \right) . \end{aligned} \quad (55)$$

A.2.3 One photon and one heavy boson fusing into a resonance

To avoid collinear singularities, we now have to impose an angular cut. In fig. 16, let ψ denote the angle between \vec{p}_1 and \vec{p}_5 in the lab frame. We impose

a symmetrical cut $\psi_0 < \psi < \pi - \psi_0$. Modelling the (complicated) photon propagator by a simple angular dependence, we may put

$$T_6 = \frac{\theta(\psi_0 < \psi < \pi - \psi_0)}{1 - \cos \psi} T_5 . \quad (56)$$

So the cross section is obtained immediately:

$$\tilde{\sigma}_6 = \frac{1}{2} \log \left(\frac{1 + \cos \psi_0}{1 - \cos \psi_0} \right) \tilde{\sigma}_5 . \quad (57)$$

A.3 Annihilation channels

Since the total energy is fixed, it is immaterial whether the boson in which the e^+e^- annihilate is a photon or a resonance (of course, for the above mentioned order of magnitude estimates one may want to put in the correct energy dependence).

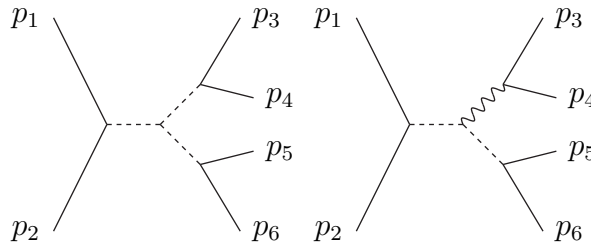


Figure 17: annihilation into two resonances Figure 18: annihilation into a photon and a resonance

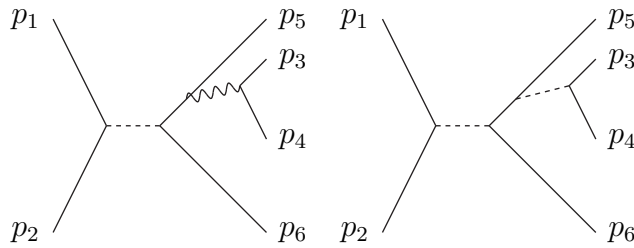


Figure 19: annihilation into a photon and two fermions Figure 20: annihilation into a resonance and two fermions

A.3.1 Annihilation into two resonances

The kinematics is given in fig. 17 and, as before, $s_i = q_i^2$. We now take

$$T_7 = \chi(s_1, s_2) \frac{s^2}{R_1(s_1)R_2(s_2)} , \quad (58)$$

where we have introduced a factor analogous to $\tau(s_1, s_2)$:

$$\chi(s_1, s_2) = \frac{s}{\lambda(s, s_1, s_2)} \theta(w_1 + w_2 < \sqrt{s_m}) , \quad s_m < s . \quad (59)$$

The cutoff is intended to avoid the singularity in λ at $w_1 + w_2 = w$. The integration is very similar to that of T_3 :

$$\begin{aligned} \tilde{\sigma}_7 &= F \left(\frac{\pi}{2} \right)^3 \frac{-s^2}{4m_1 m_2 \Gamma_1 \Gamma_2} \\ &\quad \times [A_7(z_1, z_2) - A_7(z_1, z_2^*) - A_7(z_1^*, z_2) + A_7(z_1^*, z_2^*)] , \\ A_7(z_1, z_2) &= [A_3(z_1, z_2)]_{s \rightarrow s_m} . \end{aligned} \quad (60)$$

A.3.2 Annihilation into a photon and a resonance

This channel can, strictly speaking, not occur in e^+e^- collisions, but we include it for completeness, with an eye to, for instance, electron-quark scattering. Fig. 18 gives the kinematics.

We put

$$T_8 = \chi(s_1, s_2) \frac{s \theta(s_1 > 0)}{s_1 R(s_2)} \quad (61)$$

so that we have

$$\begin{aligned} \tilde{\sigma}_8 &= F \left(\frac{\pi}{2} \right)^3 \frac{s}{2im\Gamma} [A_8(z) - A_8(z^*)] , \\ A_8(z) &= [A_2(z)]_{s \rightarrow s_m} . \end{aligned} \quad (62)$$

A.3.3 Annihilation into two fermions and a photon

This situation is given in fig. 19. A cut on $s_1 = (p_3 + p_4)^2 = q_1^2$ now automatically imposes a cut on $s_2 = (p_5 + q_1)^2$, and we may use

$$T_9 = \frac{1}{s_1 s_2} \theta(s_1 > s_0) \quad (63)$$

leading to

$$\tilde{\sigma}_9 = F \left(\frac{\pi}{2} \right)^3 \left[\frac{1}{2} \left(\log \frac{s}{s_0} \right)^2 - \left(2 + \frac{s_0}{s} \right) \log \frac{s}{s_0} + 3 \left(1 - \frac{s_0}{s} \right) \right] . \quad (64)$$

A.3.4 Annihilation into two fermions and a resonance

Replacing the photon of fig. 19 by a resonance, we obtain fig. 20. We have the following model:

$$T_{10} = \frac{s}{s_2 R(s_1)} \quad (65)$$

and

$$\begin{aligned} \tilde{\sigma}_{10} &= F \left(\frac{\pi}{2} \right)^3 \frac{s}{2im\Gamma} [A_{10}(z) - A_{10}(z^*)] \\ A_{10}(z) &= 3 - 2 \left(1 - \frac{z}{s} \right) \log \left(1 - \frac{s}{z} \right) - \left(1 + \frac{z}{s} \right) \text{Li}_2 \left(\frac{s}{z} \right) . \end{aligned} \quad (66)$$

A.4 Final state bremsstrahlung channels

In all these cases, a boson is exchanged in the t channel and a fermion pair radiated off an outgoing particle.

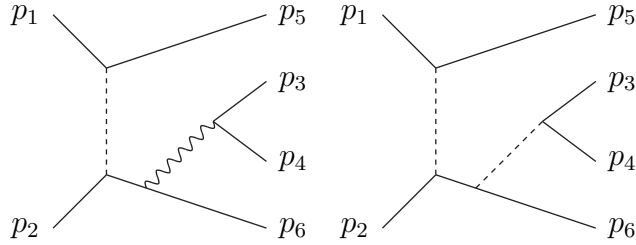


Figure 21: photon
bremsstrahlung in heavy
boson exchange

Figure 22: resonance
bremsstrahlung in heavy
boson exchange

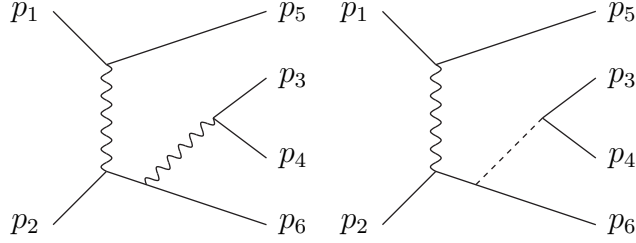


Figure 23: photon bremsstrahlung in photon exchange

Figure 24: resonance bremsstrahlung in photon exchange

A.4.1 Heavy boson exchange

If the radiated fermion pair comes from a photon, the situation is given in fig. 21. Since there is (by the definition of our model) no angular dependence arising from the boson exchange, we simply have

$$T_{11} = T_9 \quad , \quad \tilde{\sigma}_{11} = \tilde{\sigma}_9 \quad . \quad (67)$$

On the other hand, for resonance bremsstrahlung, the appropriate model for fig. 22 is again one that we have already mentioned:

$$T_{12} = T_{10} \quad , \quad \tilde{\sigma}_{12} = \tilde{\sigma}_{10} \quad . \quad (68)$$

A.4.2 Photon exchange

Now, we have a nontrivial angular dependence, which we again simply model by the scattering angle ψ between \vec{p}_1 and \vec{p}_5 , in the lab frame. For photon bremsstrahlung (fig. 23) we have a simple modification of T_{11} ;

$$\begin{aligned} T_{13} &= T_{11} \frac{\theta(\psi_0 < \psi < \pi - \psi_0)}{1 - \cos \psi} \\ \tilde{\sigma}_{13} &= \frac{1}{2} \log \left(\frac{1 + \cos \psi_0}{1 - \cos \psi_0} \right) \tilde{\sigma}_{11} \quad . \end{aligned} \quad (69)$$

Similarly, for the resonance bremsstrahlung of fig. 24:

$$\begin{aligned} T_{14} &= T_{12} \frac{\theta(\psi_0 < \psi < \pi - \psi_0)}{1 - \cos \psi} \\ \tilde{\sigma}_{14} &= \frac{1}{2} \log \left(\frac{1 + \cos \psi_0}{1 - \cos \psi_0} \right) \tilde{\sigma}_{12} \quad . \end{aligned} \quad (70)$$

A.5 Initial state bremsstrahlung

The fermion pair is radiated off an initial leg. This complicates matters somewhat.

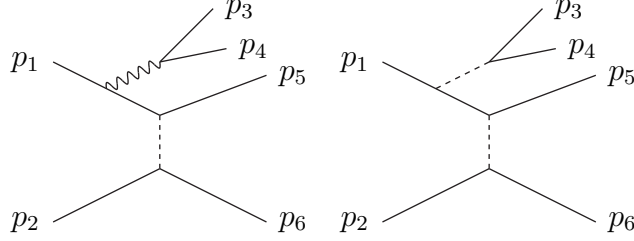


Figure 25: photon
bremsstrahlung in heavy
boson exchange

Figure 26: resonance
bremsstrahlung in heavy
boson exchange

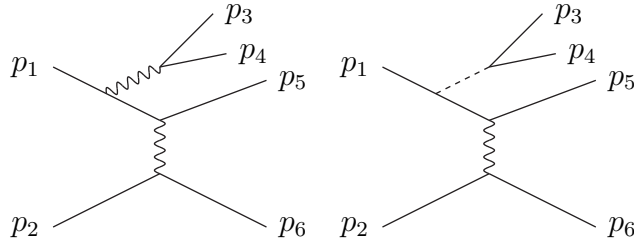


Figure 27: photon
bremsstrahlung in
photon exchange

Figure 28: resonance
bremsstrahlung in
photon exchange

A.5.1 Heavy boson exchange

Since the heavy boson propagator is again assumed to give a constant angular distribution, these channels look somewhat like the conversion channels. We define, for fig. 25 ($s_1 = q_1^2 = (p_3 + p_4)^2$, $s_2 = (p_5 + p_6)^2$, $Q^\mu = p_1^\mu - q_1^\mu$)

$$T_{15} = \frac{\tau(s_1, s_2) \theta(s_1 > s_0)}{s s_1 |Q^2|} \quad (71)$$

which leads to

$$\tilde{\sigma}_{15} = F \left(\frac{\pi}{2} \right)^3 \left[\log \frac{s}{s_0} + 1 - \frac{s_0}{s} - 4 \left(1 - \frac{w_0}{w} \right) \right] . \quad (72)$$

For fig. 26, we have, in analogy:

$$T_{16} = \frac{\tau(s_1, s_2)}{|Q^2|R(s_1)} \quad (73)$$

and

$$\begin{aligned} \tilde{\sigma}_{16} &= F \left(\frac{\pi}{2} \right)^3 \frac{1}{2im\Gamma} [A_{16}(z) - A_{16}(z^*)] \\ A_{16}(z) &= B_{16}(y) + B_{16}(-y) \\ B_{16}(y) &= (w - y)^2 \log \left(1 - \frac{w}{y} \right) - \frac{3w^2}{y} + wy \ . \end{aligned} \quad (74)$$

A.5.2 Photon exchange

For these channels, the situation is more complicated. It is straightforward to define the scattering angle ψ between \vec{p}_2 and \vec{p}_6 not in the lab frame, but in the rest frame of $\vec{p}_5 + \vec{p}_6$, but a simple cut on this angle translates to a very complicated one in the lab frame. We therefore again rely on our freedom to postulate any reasonable behaviour, and simply model the photon propagator such that it is simple in terms of this new ψ , and non singular upon integration. At small scattering angles, this is actually not a bad approximation to the real situation. For photon bremsstrahlung (fig. 27) we therefore propose

$$T_{17} = T_{15} \frac{1}{(1 - \cos \psi)^\alpha} \ , \ \alpha < 1 \ . \quad (75)$$

So that

$$\tilde{\sigma}_{17} = \left(\frac{2^{-\alpha}}{1 - \alpha} \right) \tilde{\sigma}_{15} \ . \quad (76)$$

Similarly, for the resonance bremsstrahlung of fig. 28, we use

$$\begin{aligned} T_{18} &= T_{16} \frac{1}{(1 - \cos \psi)^\alpha} \ , \\ \tilde{\sigma}_{18} &= \left(\frac{2^{-\alpha}}{1 - \alpha} \right) \tilde{\sigma}_{16} \ . \end{aligned} \quad (77)$$

Note that the algorithms used in the Monte Carlo allow us to actually generate such non-singular angular distributions without restriction on the scattering angles.

A.6 Multiperipheral scattering

We can distinguish according to the type of exchanged bosons

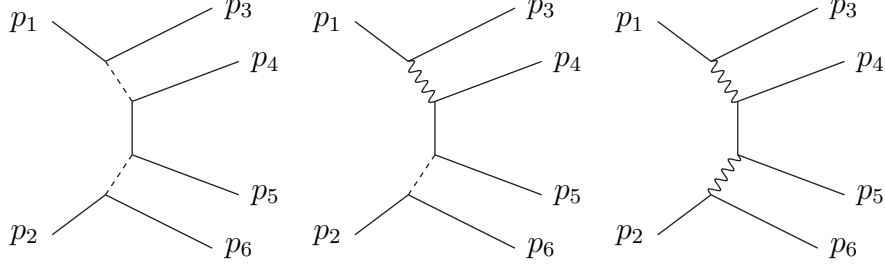


Figure 29: Two heavy bosons fusing into fermions

Figure 30: photon and heavy boson fusing into fermions

Figure 31: Two photons fusing into fermions

We shall neglect the boson propagators for simplicity. Again we are free to do this. We have $s_1 = q_1^2 = (p_3 + p_4)^2$, $s_2 = (p_5 + p_6)^2$, $Q^\mu = p_1^\mu - q_1^\mu$. For the exchange of two heavy bosons we have simply the model

$$T_{19} = \frac{\tau(s_1, s_2)}{s^2 |Q|^2}, \quad \tilde{\sigma}_{19} = F\left(\frac{\pi}{2}\right)^3 \frac{1}{6}. \quad (78)$$

Now for each photon, we apply the trick mentioned above. Let ψ_1 be the angle (\vec{p}_1, \vec{p}_3) in the $(\vec{p}_3 + \vec{p}_4)$ rest frame and ψ_2 that of (\vec{p}_2, \vec{p}_6) in the $(\vec{p}_5 + \vec{p}_6)$ rest frame. Then, for fig. 30 and 31 respectively, we write

$$\begin{aligned} T_{20} &= T_{19} \frac{1}{(1 - \cos \psi_1)^\alpha}, \quad \tilde{\sigma}_{20} = \left(\frac{2^{-\alpha}}{1 - \alpha}\right) \tilde{\sigma}_{19} \\ T_{21} &= T_{20} \frac{1}{(1 - \cos \psi_2)^\alpha}, \quad \tilde{\sigma}_{21} = \left(\frac{2^{-\alpha}}{1 - \alpha}\right) \tilde{\sigma}_{20}. \end{aligned} \quad (79)$$

This finishes our list of matrix element models.

References

- [1] K. Hagiwara, in: *Physics and Experiments with Linear Colliders*, R. Orava, P. Eerola, and M. Nordberg, eds. (World Scientific, Singapore, 1992) p.387.
- [2] S. Katsanevas et al. DELPHI 92-166 PHYS. (1992) 250.
- [3] T. Barklow, in: *Physics and Experiments with Linear Colliders*, R. Orava, P. Eerola, and M. Nordberg, eds. (World Scientific, Singapore, 1992) p.423;
F. Boudjema and F. Renard, in : *e^+e^- Collisions at 500 GeV: the Physics Potential*, P. Zerwas, ed. (DESY 92-123) p.721;
G. Gounaris *et al.*, *ibidem*, p.735;
G. Bélanger and F. Boudjema, *ibidem*, p.763, p.783;
S.Y. Choi and F. Schrempp, *ibidem*, p.793;
S. Ambrosiano and B. Mele, *ibidem*, p.211;
see also the references quoted in the above papers.
- [4] W. Beenakker, K. Kolodziej and T. Sack, Phys. Lett. **B258** (1991) 469.
- [5] M. Böhm et al., Nucl. Phys. **B304** (1988) 463;
J. Fleischer, F. Jegerlehner and M. Zralek, Z. Phys. **C42** (1989) 409;
A. Denner and T. Sack, Nucl. Phys. **B306** (1988) 221.
- [6] For a review see R. Gastmans and T. T. Wu, *The ubiquitous photon, helicity methods for QED and QCD*, Clarendon Press, Oxford, 1990.
- [7] R. Kleiss and W. J. Stirling, Nucl. Phys. **B262** (1985) 235.
- [8] F. A. Berends and W. T. Giele, Nucl. Phys. **B294** (1987) 700.
- [9] F. A. Berends, P. H. Daverveldt and R. Kleiss, Nucl. Phys. **B253** (1985) 441; Comp. Phys. Comm. **40** (1986) 285;
P. H. Daverveldt, Ph. D. thesis, Leiden (1985).
- [10] J. Hilgart, R. Kleiss and F. Le Diberder, Comp. Phys. Comm. **75** (1993) 191.
- [11] A. Aeppli, F. Cuypers and G.J. van Oldenborgh, Phys. Lett. **B314** (1993) 413.

- [12] P. Kalyniak, P. Madsen and N. Sinha, Phys. Rev. **D48** (1993) 5081.
- [13] T. Ishikawa *et al.*, KEK 92-10, to be published in the Proceedings of the VIIth Workshop on High Energy Physics and Quantum Field Theory, Sochi, Russia, 1992.
- [14] G. Couture and S. Godfrey, OCIP/C 93-18, UQAM-PHE-9306.
- [15] D. Bardin, M. Bilenky, A. Olchevski and T. Riemann, in preparation.
- [16] F. A. Berends, R. Kleiss and R. Pittau, in preparation.

label	final state	N_a	N_n	total	N_b	signals
1	$e^+e^-\nu_e\bar{\nu}_e$	48	8	56	12	1 2 3 4 5
2	$e^-\bar{\nu}_e\nu_\mu\mu^+$	14	4	18	3	1 3
3	$e^-\bar{\nu}_e\nu_\tau\tau^+$					
4	$\nu_e e^+\mu^-\bar{\nu}_\mu$					
5	$\nu_e e^+\tau^-\bar{\nu}_\tau$					
6	$\mu^+\mu^-\nu_\mu\bar{\nu}_\mu$	17	2	19	0	1 2
7	$\tau^+\tau^-\nu_\tau\bar{\nu}_\tau$					
8	$\mu^-\bar{\nu}_\mu\nu_\tau\tau^+$	7	2	9	0	1
9	$\tau^-\bar{\nu}_\tau\nu_\mu\mu^+$					
10	$e^+e^-e^+e^-$	144	0	144	84	2 4
11	$e^+e^-\mu^+\mu^-$	48	0	48	26	2 4
12	$e^+e^-\tau^+\tau^-$					
13	$\mu^+\mu^-\mu^+\mu^-$	48	0	48	20	2
14	$\tau^+\tau^-\tau^+\tau^-$					
15	$\mu^+\mu^-\tau^+\tau^-$	24	0	24	10	2
16	$e^+e^-\nu_\mu\bar{\nu}_\mu$	20	0	20	2	2 4
17	$e^+e^-\nu_\tau\bar{\nu}_\tau$					
18	$\nu_e\bar{\nu}_e\mu^+\mu^-$	17	2	19	4	2 5
19	$\nu_e\bar{\nu}_e\tau^+\tau^-$					
20	$\nu_\tau\bar{\nu}_\tau\mu^+\mu^-$	10	0	10	0	2
21	$\nu_\mu\bar{\nu}_\mu\tau^+\tau^-$					
22	$\nu_e\bar{\nu}_e\nu_e\bar{\nu}_e$	32	4	36	4	2 5
23	$\nu_e\bar{\nu}_e\nu_\mu\bar{\nu}_\mu$	11	1	12	1	2
24	$\nu_e\bar{\nu}_e\nu_\tau\bar{\nu}_\tau$					
25	$\nu_\mu\bar{\nu}_\mu\nu_\mu\bar{\nu}_\mu$	12	0	12	0	2 5
26	$\nu_\tau\bar{\nu}_\tau\nu_\tau\bar{\nu}_\tau$					
27	$\nu_\mu\bar{\nu}_\mu\nu_\tau\bar{\nu}_\tau$	6	0	6	0	2

Table 1: leptonic four-fermion final states in e^+e^- collisions.

label	final state	N_a	N_n	total	N_b	signals
1	$e^- \bar{\nu}_e u \bar{d}$	16	4	20	4	1 3
2	$e^- \bar{\nu}_e c \bar{s}$					
3	$\nu_e e^+ d \bar{u}$					
4	$\nu_e e^+ s \bar{c}$					
5	$\mu^- \bar{\nu}_\mu u \bar{d}$	8	2	10	0	1
6	$\mu^- \bar{\nu}_\mu c \bar{s}$					
7	$\mu^+ \nu_\mu d \bar{u}$					
8	$\mu^+ \nu_\mu s \bar{c}$					
9	$\tau^- \bar{\nu}_\tau u \bar{d}$					
10	$\tau^- \bar{\nu}_\tau c \bar{s}$					
11	$\tau^+ \nu_\tau d \bar{u}$					
12	$\tau^+ \nu_\tau s \bar{c}$					
13	$e^+ e^- u \bar{u}$	48	0	48	26	2 4
14	$e^+ e^- c \bar{c}$					
15	$e^+ e^- d \bar{d}$	48	0	48	26	2 4
16	$e^+ e^- s \bar{s}$					
17	$e^+ e^- b \bar{b}$					
18	$\mu^+ \mu^- u \bar{u}$	24	0	24	10	2
19	$\mu^+ \mu^- c \bar{c}$					
20	$\tau^+ \tau^- u \bar{u}$					
21	$\tau^+ \tau^- c \bar{c}$					

Table 2: semileptonic four-fermion final states in e^+e^- collisions (*continued on next page*).

label	final state	N_a	N_n	total	N_b	signals
22	$\mu^+\mu^-d\bar{d}$	24	0	24	10	2
23	$\mu^+\mu^-s\bar{s}$					
24	$\mu^+\mu^-b\bar{b}$					
25	$\tau^+\tau^-d\bar{d}$					
26	$\tau^+\tau^-s\bar{s}$					
27	$\tau^+\tau^-b\bar{b}$					
28	$\nu_e\bar{\nu}_e u\bar{u}$					
29	$\nu_e\bar{\nu}_e c\bar{c}$					
30	$\nu_e\bar{\nu}_e d\bar{d}$	17	2	19	4	2 5
31	$\nu_e\bar{\nu}_e s\bar{s}$					
32	$\nu_e\bar{\nu}_e b\bar{b}$					
33	$\nu_\mu\bar{\nu}_\mu u\bar{u}$	10	0	10	0	2
34	$\nu_\mu\bar{\nu}_\mu c\bar{c}$					
35	$\nu_\tau\bar{\nu}_\tau u\bar{u}$					
36	$\nu_\tau\bar{\nu}_\tau c\bar{c}$					
37	$\nu_\mu\bar{\nu}_\mu d\bar{d}$	10	0	10	0	2
38	$\nu_\mu\bar{\nu}_\mu s\bar{s}$					
39	$\nu_\mu\bar{\nu}_\mu b\bar{b}$					
40	$\nu_\tau\bar{\nu}_\tau d\bar{d}$					
41	$\nu_\tau\bar{\nu}_\tau s\bar{s}$					
42	$\nu_\tau\bar{\nu}_\tau b\bar{b}$					

Table 2: semileptonic four-fermion final states in e^+e^- collisions (*continued from previous page*).

label	final state	N_a	N_n	total	N_b	signals
1	$u\bar{u}d\bar{d}$	33	2	35	2	1 2
2	$c\bar{c}d\bar{d}$					
3	$u\bar{d}s\bar{c}$	9	2	11	0	1
4	$d\bar{u}c\bar{s}$					
5	$u\bar{u}u\bar{u}$	48	0	48	20	2
6	$c\bar{c}c\bar{c}$					
7	$d\bar{d}d\bar{d}$	48	0	48	20	2
8	$s\bar{s}s\bar{s}$					
9	$b\bar{b}b\bar{b}$					
10	$u\bar{u}c\bar{c}$	24	0	24	10	2
11	$u\bar{u}s\bar{s}$	24	0	24	10	2
12	$u\bar{u}b\bar{b}$					
13	$c\bar{c}d\bar{d}$					
14	$c\bar{c}b\bar{b}$					
15	$d\bar{d}s\bar{s}$	24	0	24	10	2
16	$d\bar{d}b\bar{b}$					
17	$s\bar{s}b\bar{b}$					

Table 3: hadronic four-fermion final states in e^+e^- collisions.

	$\sqrt{s} = 165 \text{ GeV}$	$\sqrt{s} = 175 \text{ GeV}$	$\sqrt{s} = 185 \text{ GeV}$	$\sqrt{s} = 195 \text{ GeV}$
An.	11.95	18.48	20.41	20.82
M. C.	11.96 ± 0.03	18.45 ± 0.04	20.40 ± 0.05	20.79 ± 0.05

Table 4: analytic vs. Monte Carlo W-pair signal (in picobarns).

Here $\alpha = 1/129$, $M_W = 80.5 \text{ GeV}$, $M_Z = 91.9 \text{ GeV}$, $\cos \theta_W = M_W/M_Z$ and $\Gamma_W = (3\alpha M_W)/(4 \sin^2 \theta_W)$. The zero width extrapolated values of M.C. are obtained with the substitutions $\Gamma_W \rightarrow \Gamma_W/N$ and $\sigma \rightarrow \sigma/N^2$, by taking the numerical limit for growing N.

process	$\sqrt{s} = 150 \text{ GeV}$	$\sqrt{s} = 175 \text{ GeV}$	$\sqrt{s} = 200 \text{ GeV}$	$\sqrt{s} = 500 \text{ GeV}$
W-pair	.3600 10^{-2} .0011	.1181 .0002	.1304 .0003	.2130 10^{-1} .0011
$e^+e^-\nu_e\bar{\nu}_e$.2949 10^{-2} .0008	.1208 .0002	.1466 .0003	.6111 10^{-1} .0028
$\mu^+\mu^-\nu_\mu\bar{\nu}_\mu$.4350 10^{-2} .0012	.1196 .0002	.1364 .0003	.2209 10^{-1} .0011
$e^+e^-\nu_\mu\bar{\nu}_\mu$.8379 10^{-3} .0026	.1906 10^{-2} .0004	.6226 10^{-2} .0008	.2342 10^{-2} .0006
$\nu_\tau\bar{\nu}_\tau\mu^+\mu^-$.7927 10^{-3} .0031	.1342 10^{-2} .0003	.5457 10^{-2} .0007	.1054 10^{-2} .0003
$\nu_e\bar{\nu}_e\mu^+\mu^-$.1002 10^{-2} .0004	.1842 10^{-2} .0005	.6004 10^{-2} .0009	.7660 10^{-2} .0079
W-pair	.3598 10^{-2} .0011	.1187 .0002	.1315 .0003	.2130 10^{-1} .0011
$e^-\bar{\nu}_e\nu_\mu\mu^+$.2912 10^{-2} .0008	.1192 .0002	.1359 .0003	.3598 10^{-1} .0014
$\mu^-\bar{\nu}_\mu\nu_\tau\tau^+$.3649 10^{-2} .0010	.1193 .0002	.1307 .0003	.2101 10^{-1} .0010

Table 5: leptonic cross sections in picobarns. The second line of each entry is the Monte Carlo error. In the first six entries $m_{(e^+e^-)}, m_{(\mu^+\mu^-)} > 10 \text{ GeV}$, $|\cos\theta_{e^\pm, \mu^\pm}| < 0.9$ (θ is the scattering angle), $E_{e^\pm, \mu^\pm} > 20 \text{ GeV}$. In the last three ones $E_{e^-, \mu^\pm, \tau^+} > 20 \text{ GeV}$, $|\cos\theta_{e^-, \mu^\pm, \tau^+}| < 0.9$.

process	$\sqrt{s} = 150 \text{ GeV}$	$\sqrt{s} = 175 \text{ GeV}$	$\sqrt{s} = 200 \text{ GeV}$	$\sqrt{s} = 500 \text{ GeV}$
W-pair	.9605 10^{-2} .0030	.3342 .0007	.3601 .0008	.4682 10^{-1} .0028
$e^- \bar{\nu}_e u \bar{d}$.7563 10^{-2} .0021	.3345 .0007	.3745 .0009	.8293 10^{-1} .0035
$\mu^- \bar{\nu}_\mu u \bar{d}$.9728 10^{-2} .0028	.3337 .0007	.3610 .0008	.4599 10^{-1} .0024

Table 6: semileptonic cross sections (in pb). $E_{e^-, \mu^-, u, \bar{d}} > 20 \text{ GeV}$, $|\cos \theta_{e^-, \mu^-, u, \bar{d}}| < 0.9$, $|\cos \angle(u, \bar{d})| < 0.9$, $m(u\bar{d}) > 10 \text{ GeV}$.

	$\sqrt{s} = 190 \text{ GeV}$	$\sqrt{s} = 200 \text{ GeV}$	$\sqrt{s} = 500 \text{ GeV}$
W-pair	.3532 .0009	.3419 .0008	.2498 10^{-1} .0018
1 cut	.3612 .0009	.3550 .0009	.3522 10^{-1} .0020
W-pair	.3392 .0009	.3259 .0009	.2236 10^{-1} .0014
2 cuts	.3407 .0009	.3292 .0009	.2228 10^{-1} .0014

Table 7: $e^- (3) \bar{\nu}_e (4) u (5) \bar{d} (6)$ cross section in picobarns. The 1st entry is a comparison between the WW signal and the full result with a cut $70 < m_{(56)} < 90 \text{ GeV}$. In the 2nd entry $70 < m_{(34)}, m_{(56)} < 90 \text{ GeV}$. All the other cuts are like in table 6, except that an energy cut $E_{e^-, u, \bar{d}} > 50 \text{ GeV}$ is required at $\sqrt{s} = 500 \text{ GeV}$.

process	$\sqrt{s} = 150 \text{ GeV}$	$\sqrt{s} = 175 \text{ GeV}$	$\sqrt{s} = 200 \text{ GeV}$	$\sqrt{s} = 500 \text{ GeV}$
W-pair	.2141 10^{-1} .0019	.7699 .0018	.8726 .0023	.1083 .0008
$u\bar{u}d\bar{d}$.2317 10^{-1} .0010	.7745 .0018	.8987 .0023	.1103 .0006
$u\bar{d}s\bar{c}$.2132 10^{-1} .0010	.7720 .0018	.8709 .0023	.1052 .0006
$u\bar{u}u\bar{u}$.1033 10^{-2} .0008	.1956 10^{-2} .0006	.1031 10^{-1} .0002	.1845 10^{-2} .0006
$d\bar{d}d\bar{d}$.3900 10^{-3} .0018	.1171 10^{-2} .0003	.1508 10^{-1} .0003	.2239 10^{-2} .0008
$u\bar{u}c\bar{c}$.2417 10^{-2} .0012	.4032 10^{-2} .0014	.2066 10^{-1} .0004	.3715 10^{-2} .0013
$u\bar{u}s\bar{s}$.1836 10^{-2} .0009	.3474 10^{-2} .0011	.2499 10^{-1} .0005	.4143 10^{-2} .0014
$d\bar{d}s\bar{s}$.8245 10^{-3} .0038	.2437 10^{-2} .0007	.3026 10^{-1} .0006	.4475 10^{-2} .0017

Table 8: hadronic cross sections (in pb). $E_{(all \text{ particles})} > 20 \text{ GeV}$, $|\cos \theta_{(all \text{ particles})}| < 0.9$. Moreover $m_{(ij)} > 10 \text{ GeV}$ and $|\cos \angle_{(i,j)}| < 0.9$ between all possible final state couples.

m_W (34)	m_W (56)	m_Z (36)	m_Z (45)	cross section (pb)
0	0	0	0	$.6362 \pm .0017 \cdot 10^{-2}$
0	0	0	1	$.1550 \pm .0007 \cdot 10^{-2}$
0	0	1	0	$.5938 \pm .0024 \cdot 10^{-2}$
0	0	1	1	$.4144 \pm .0038 \cdot 10^{-3}$
0	1	0	0	$.1441 \pm .0002 \cdot 10^{-1}$
0	1	0	1	$.7142 \pm .0045 \cdot 10^{-3}$
0	1	1	0	$.8217 \pm .0075 \cdot 10^{-3}$
0	1	1	1	$.2219 \pm .0089 \cdot 10^{-4}$
1	0	0	0	$.1441 \pm .0002 \cdot 10^{-1}$
1	0	0	1	$.7194 \pm .0045 \cdot 10^{-3}$
1	0	1	0	$.8162 \pm .0074 \cdot 10^{-3}$
1	0	1	1	$.2197 \pm .0086 \cdot 10^{-4}$
1	1	0	0	$.1318 \pm .0003 \cdot 10^{-1}$
1	1	0	1	$.6840 \pm .0066 \cdot 10^{-3}$
1	1	1	0	$.1065 \pm .0011 \cdot 10^{-3}$
1	1	1	1	0 events

Table 9: invariant mass analysis on e^- (3) $\bar{\nu}_e$ (4) ν_e (5) e^+ (6) at $\sqrt{s} = 500 \text{ GeV}$. In the first four columns a number 1 is written when the invariant mass m_V (ij) is inside the interval $M_V - 2\Gamma_V < m_V$ (ij) $< M_V + 2\Gamma_V$ ($V= Z,W$), otherwise the corresponding entry is 0. Additional cuts are $E_{e^+, e^-} > 20 \text{ GeV}$, $|\cos \theta_{e^+, e^-}| < 0.9$, $m_{(e^+e^-)} > 30 \text{ GeV}$.

	$\sqrt{s} = 500 \text{ GeV}$	$\sqrt{s} = 1000 \text{ GeV}$	$\sqrt{s} = 2000 \text{ GeV}$
$\sigma_{(1)}$	$.2127 \pm .0002 \ 10^{-1}$	$.5885 \pm .0010 \ 10^{-2}$	$.2045 \pm .0009 \ 10^{-2}$
$\hat{\sigma}_{(1)}$	$.1317 \pm .0002 \ 10^{-1}$	$.3324 \pm .0005 \ 10^{-2}$	$.8707 \pm .0022 \ 10^{-3}$
$\hat{\sigma}_{tot(1)}$	$.1318 \pm .0003 \ 10^{-1}$	$.3339 \pm .0022 \ 10^{-2}$	$.8917 \pm .0145 \ 10^{-3}$
$\sigma_{(2)}$	$.6319 \pm .0004 \ 10^{-3}$	$.1548 \pm .0002 \ 10^{-3}$	$.4427 \pm .0010 \ 10^{-4}$
$\hat{\sigma}_{(2)}$	$.3921 \pm .0003 \ 10^{-3}$	$.9426 \pm .0009 \ 10^{-4}$	$.2589 \pm .0003 \ 10^{-4}$
$\hat{\sigma}_{tot(2)}$	$.4144 \pm .0038 \ 10^{-3}$	$.1009 \pm .0015 \ 10^{-3}$	$.2689 \pm .0077 \ 10^{-4}$
$\sigma_{(3)}$	$.1169 \pm .0001 \ 10^{-1}$	$.1201 \pm .0001 \ 10^{-1}$	$.7250 \pm .0018 \ 10^{-2}$
$\hat{\sigma}_{(3)}$	$.8969 \pm .0007 \ 10^{-2}$	$.9483 \pm .0009 \ 10^{-2}$	$.5601 \pm .0007 \ 10^{-2}$
$\hat{\sigma}_{tot(3)}$	$.1441 \pm .0002 \ 10^{-1}$	$.1161 \pm .0004 \ 10^{-1}$	$.6126 \pm .0037 \ 10^{-2}$
$\sigma_{(4)}$	$.1760 \pm .0001 \ 10^{-2}$	$.1159 \pm .0001 \ 10^{-2}$	$.6167 \pm .0004 \ 10^{-3}$
$\hat{\sigma}_{(4)}$	$.1379 \pm .0001 \ 10^{-2}$	$.9449 \pm .0005 \ 10^{-3}$	$.5103 \pm .0004 \ 10^{-3}$
$\hat{\sigma}_{tot(4)}$	$.1550 \pm .0007 \ 10^{-2}$	$.1015 \pm .0009 \ 10^{-2}$	$.5281 \pm .0060 \ 10^{-3}$
$\sigma_{(5)}$	$.6840 \pm .0013 \ 10^{-2}$	$.1732 \pm .0009 \ 10^{-1}$	$.3038 \pm .0066 \ 10^{-1}$
$\hat{\sigma}_{(5)}$	$.5327 \pm .0012 \ 10^{-2}$	$.1382 \pm .0007 \ 10^{-1}$	$.2233 \pm .0031 \ 10^{-1}$
$\hat{\sigma}_{tot(5)}$	$.5938 \pm .0024 \ 10^{-2}$	$.1411 \pm .0008 \ 10^{-1}$	$.2275 \pm .0031 \ 10^{-1}$
$\sum_i \sigma_{(i)}$	$.4219 \pm .0004 \ 10^{-1}$	$.3653 \pm .0010 \ 10^{-1}$	$.4033 \pm .0069 \ 10^{-1}$
σ_{tot}	$.6017 \pm .0005 \ 10^{-1}$	$.5099 \pm .0011 \ 10^{-1}$	$.4459 \pm .0035 \ 10^{-1}$

Table 10: cross sections for $e^+e^-\nu_e\bar{\nu}_e$ in picobarns. $\sigma_{(i)}$ are the cross sections for the processes (1)-(5) (see introduction) computed including only the signal diagrams. $\hat{\sigma}_{(i)}$ are the corresponding cross sections reconstructed using an invariant mass analysis (see caption of table 9). In σ_{tot} all diagrams are included and $\hat{\sigma}_{tot(i)}$ are the results of the invariant mass analysis on σ_{tot} . $E_{e^+, e^-} > 20 \text{ GeV}$, $|\cos\theta_{e^+, e^-}| < 0.9$, $m_{(e^+e^-)} > 30 \text{ GeV}$.

	$\sqrt{s} = 500 \text{ GeV}$	$\sqrt{s} = 1000 \text{ GeV}$	$\sqrt{s} = 2000 \text{ GeV}$
$\sigma_{(1)}$	$.4702 \pm .0006 \ 10^{-1}$	$.1428 \pm .0003 \ 10^{-1}$	$.5460 \pm .0025 \ 10^{-2}$
$\hat{\sigma}_{(1)}$	$.2823 \pm .0004 \ 10^{-1}$	$.7907 \pm .0014 \ 10^{-2}$	$.2272 \pm .0006 \ 10^{-2}$
$\hat{\sigma}_{tot(1)}$	$.2822 \pm .0005 \ 10^{-1}$	$.7920 \pm .0020 \ 10^{-2}$	$.2275 \pm .0003 \ 10^{-2}$
$\sigma_{(3)}$	$.2961 \pm .0002 \ 10^{-1}$	$.2953 \pm .0003 \ 10^{-1}$	$.1817 \pm .0001 \ 10^{-1}$
$\hat{\sigma}_{(3)}$	$.2279 \pm .0002 \ 10^{-1}$	$.2348 \pm .0002 \ 10^{-1}$	$.1417 \pm .0001 \ 10^{-1}$
$\hat{\sigma}_{tot(3)}$	$.3516 \pm .0004 \ 10^{-1}$	$.2836 \pm .0003 \ 10^{-1}$	$.1559 \pm .0001 \ 10^{-1}$
$\sum_i \sigma_{(i)}$	$.7663 \pm .0008 \ 10^{-1}$	$.4381 \pm .0006 \ 10^{-1}$	$.2363 \pm .0004 \ 10^{-1}$
σ_{tot}	$.8273 \pm .0007 \ 10^{-1}$	$.4520 \pm .0004 \ 10^{-1}$	$.2192 \pm .0001 \ 10^{-1}$

Table 11: cross sections for $e^- \bar{\nu}_e u \bar{d}$ (pb). See caption of table 10. $E_{e^-, u, \bar{d}} > 20 \text{ GeV}$, $|\cos \theta_{e^-, u, \bar{d}}| < 0.9$, $m_{(u\bar{d})} > 30 \text{ GeV}$.

	$\sqrt{s} = 500 \text{ GeV}$	$\sqrt{s} = 1000 \text{ GeV}$	$\sqrt{s} = 2000 \text{ GeV}$
$\sigma_{(2)}$	$.7298 \pm .0002 \ 10^{-3}$	$.2074 \pm .0001 \ 10^{-3}$	$.6386 \pm .0004 \ 10^{-4}$
$\hat{\sigma}_{(2)}$	$.4536 \pm .0001 \ 10^{-3}$	$.1301 \pm .0001 \ 10^{-3}$	$.3930 \pm .0002 \ 10^{-4}$
$\hat{\sigma}_{tot(2)}$	$.4765 \pm .0008 \ 10^{-3}$	$.1351 \pm .0003 \ 10^{-3}$	$.4015 \pm .0012 \ 10^{-4}$
$\sigma_{(4)}$	$.1725 \pm .0001 \ 10^{-2}$	$.9679 \pm .0002 \ 10^{-3}$	$.4775 \pm .0001 \ 10^{-3}$
$\hat{\sigma}_{(4)}$	$.1354 \pm .0001 \ 10^{-2}$	$.7874 \pm .0002 \ 10^{-3}$	$.3924 \pm .0001 \ 10^{-3}$
$\hat{\sigma}_{tot(4)}$	$.1361 \pm .0001 \ 10^{-2}$	$.7895 \pm .0006 \ 10^{-3}$	$.3919 \pm .0003 \ 10^{-3}$
$\sum_i \sigma_{(i)}$	$.2455 \pm .0001 \ 10^{-2}$	$.1175 \pm .0001 \ 10^{-2}$	$.5414 \pm .0001 \ 10^{-3}$
σ_{tot}	$.2833 \pm .0001 \ 10^{-2}$	$.1398 \pm .0001 \ 10^{-2}$	$.6471 \pm .0004 \ 10^{-3}$

Table 12: cross sections for $e^+ e^- u \bar{u}$ in picobarns. See caption of table 10. $E_{(all \ particles)} > 20 \text{ GeV}$, $|\cos \theta_{(all \ particles)}| < 0.9$, $m_{(u\bar{u})}, m_{(e^+e^-)} > 30 \text{ GeV}$.

	$\sqrt{s} = 500 \text{ GeV}$	$\sqrt{s} = 1000 \text{ GeV}$	$\sqrt{s} = 2000 \text{ GeV}$
$\sigma_{(2)}$	$.2165 \pm .0001 \ 10^{-2}$	$.5306 \pm .0006 \ 10^{-3}$	$.1507 \pm .0003 \ 10^{-3}$
$\hat{\sigma}_{(2)}$	$.1334 \pm .0001 \ 10^{-2}$	$.3219 \pm .0003 \ 10^{-3}$	$.8848 \pm .0013 \ 10^{-4}$
$\hat{\sigma}_{tot(2)}$	$.1364 \pm .0006 \ 10^{-2}$	$.3273 \pm .0045 \ 10^{-3}$	$.9275 \pm .0282 \ 10^{-4}$
$\sigma_{(5)}$	$.2242 \pm .0005 \ 10^{-1}$	$.5795 \pm .0029 \ 10^{-1}$	$.1331 \pm .0324$
$\hat{\sigma}_{(5)}$	$.1749 \pm .0004 \ 10^{-1}$	$.4601 \pm .0025 \ 10^{-1}$	$.7631 \pm .0101 \ 10^{-1}$
$\hat{\sigma}_{tot(5)}$	$.1680 \pm .0004 \ 10^{-1}$	$.4554 \pm .0025 \ 10^{-1}$	$.7781 \pm .0104 \ 10^{-1}$
$\sum_i \sigma_{(i)}$	$.2459 \pm .0005 \ 10^{-1}$	$.5848 \pm .0029 \ 10^{-1}$	$.1333 \pm .0324$
σ_{tot}	$.2374 \pm .0004 \ 10^{-1}$	$.5663 \pm .0027 \ 10^{-1}$	$.9301 \pm .0110 \ 10^{-1}$

Table 13: Cross sections for $\nu_e \bar{\nu}_e u \bar{u}$ (pb). See caption of table 10. $E_u, \bar{u} > 20 \text{ GeV}$, $|\cos \theta_u, \bar{u}| < 0.9$, $m(u\bar{u}) > 30 \text{ GeV}$.